



NIH Public Access

Author Manuscript

Biochemistry. Author manuscript; available in PMC 2013 October 02.

Published in final edited form as:

Biochemistry. 2012 October 2; 51(39): 7699–7711. doi:10.1021/bi301026c.

TURNOVER-DEPENDENT COVALENT INACTIVATION OF *Staphylococcus aureus* COENZYME A-DISULFIDE REDUCTASE BY COENZYME A-MIMETICS: MECHANISTIC AND STRUCTURAL INSIGHTS^{†,‡}

Bret D. Wallace^{||,§}, Jonathan S. Edwards^{||,§,⊥}, Jamie R. Wallen^{#,△}, Wessel J.A. Moolman[@], Renier van der Westhuyzen[@], Erick Strauss^{*,@}, Matthew R. Redinbo^{*§}, and Al Claiborne^{*#}
Departments of Chemistry and Biochemistry and Biophysics, University of North Carolina at Chapel Hill, Chapel Hill, North Carolina 27599-3290, Center for Structural Biology, Wake Forest School of Medicine, Winston-Salem, North Carolina 27157, and Department of Biochemistry, Stellenbosch University, Matieland 7602, South Africa

Abstract

Disruption of the unusual thiol-based redox homeostasis mechanisms in *Staphylococcus aureus* represents a unique opportunity to identify new metabolic processes, and new targets for intervention. Targeting uncommon aspects of CoASH biosynthetic and redox functions in *S. aureus*, the antibiotic CJ-15,801 has recently been demonstrated to be an antimetabolite of the CoASH biosynthetic pathway in this organism; CoAS-mimetics containing α,β-unsaturated sulfone and carboxyl moieties have also been exploited as irreversible inhibitors of *S. aureus* coenzyme A-disulfide reductase (*SaCoADR*). In this work we have determined the crystal structures of three of these covalent *SaCoADR*-inhibitor complexes, prepared by inactivation of wild-type enzyme during turnover. The structures reveal the covalent linkage between the active-site Cys43-S_γ and C_β of the vinyl sulfone or carboxyl moiety. The full occupancy of two inhibitor molecules per enzyme dimer, together with kinetic analyses of the wild-type/C43S heterodimer, indicates that half-sites-reactivity is not a factor during normal catalytic turnover. Further, we provide the structures of *SaCoADR* active-site mutants; in particular, Tyr419'-OH plays dramatic roles in directing intramolecular reduction of the Cys43-SSCoA redox center, in the redox asymmetry observed for the two FAD per dimer in NADPH titrations, and in catalysis. The two conformations observed for the Ser43 side chain in the C43S mutant structure lend support to a conformational switch for Cys43-S_γ during its catalytic Cys43-SSCoA/Cys43-SH redox cycle. Finally, the structures of the three inhibitor complexes provide a framework for design of more effective inhibitors with therapeutic potential against several major bacterial pathogens.

[†]This work was supported by National Institutes of Health (NIH) Grant AI-078924 (M.R.R.), by North Carolina Biotechnology Center Grant 2011-MRG-1116 (A.C.), by National Research Foundation (NRF) grant CPR2011072600022216 (E.S.) and by a grant from the Medical Research Council (E.S.). W.J.A.M and R.v.d.W. were recipients of NRF Scarce Skills scholarships.

[‡]Coordinates have been deposited with the Protein Data Bank under the file names 4EQX, 4EQR, 4EQS, 4EQW, 4EM4, 4EM3, and 4EMW.

^{*}To whom correspondence should be addressed. Tel.: +27-21-808-5866, Fax: +27-21-808-5863 (E.S.); Tel.: (919) 843-8910; Fax: (919) 962-2388 (M.R.R.); Tel.: (336) 716-3914, Fax: (336) 713-1283 (A.C.). estrauss@sun.ac.za; redinbo@unc.edu; alc@csb.wfu.edu.

^{||}These authors contributed equally to this work.

[§]University of North Carolina at Chapel Hill.

[#]Wake Forest School of Medicine.

[@]Stellenbosch University.

[⊥]Present address: Department of Biological Engineering, Massachusetts Institute of Technology, Cambridge, MA 02139.

[△]Present address: Department of Biochemistry and Molecular Biophysics, Washington University, School of Medicine, St. Louis, MO 63110.

\$watermark-text

\$watermark-text

\$watermark-text

The “thiolome” has been referred to as the proteome-wide redox state of cysteine residues (1). Coenzyme A-disulfide reductase (CoADR),¹ other Flavoprotein Disulfide Reductases, and the Thioredoxin Fold Proteins that include the putative bacilliredoxin, YphP, account for a major portion of the thiolomes in *Staphylococcus aureus* and *Bacillus anthracis* (2–6). We extend the definition of the thiolome to apply to the diversity in the structure, function, and distribution of low-molecular-weight thiols — the metabolite-based thiolome. CoASH and the recently identified bacillithiol (7) function together with the protein-based thiolome to maintain redox homeostasis in these organisms (6). Bioinformatics analyses (8) have classified Flavoprotein Disulfide Reductases into three subgroups: the *Disulfide Reductases* that include GR, the *Alkyl Hydroperoxide Reductases* that include thioredoxin reductase, and the *Peroxidase-Oxidase-Reductases* that include CoADR, the CoADR-RHD isoform — which contains a C-terminal rhodanese homology domain, as characterized in *B. anthracis* (9) and *Shewanella loihica* (10) — and the *Pelobacter carbinolicus* “NAD(FAD)-dependent dehydrogenase” isoform encoded by the Pcar_0429 locus (11). In spite of clear similarities with regard to the reactions that they catalyze, the CoADR enzymes are mechanistically distinct from the *Disulfide Reductase* subgroup enzymes, in that a single active-site cysteine (*SaCoADR* Cys43 and *BaCoADR* Cys42, respectively) reacts with the (CoAS)₂ substrate to form a Cys-SSCoA mixed disulfide redox center, which represents the resting state of the enzyme and is reduced by NAD(P)H *via* the flavin cofactor in the catalytic cycle (12, 13).

Kinetic and structural analyses of the *SaCoADR* and *BaCoADR* enzymes have revealed several important features relevant to catalysis. Detailed equilibrium titration studies have demonstrated significant asymmetric behavior for both *SaCoADR* (13) and *BaCoADR* (2), which occur as homodimeric enzymes. NADPH titrations of *SaCoADR* lead to an asymmetric EH₂·NADPH/EH₄·NADP⁺ complex in which only one FAD/dimer is reduced (Scheme 1). However, crystal structures of *SaCoADR* (14) and *BaCoADR* (2), in oxidized form and in the reduced *BaCoADR* EH₂·CoASH-NAD(P)H complex, provide no structural basis for such asymmetric behavior with NAD(P)H. In a recent study CoAS-mimetics were designed and used to inactivate *SaCoADR* by conjugate addition of the Cys43-thiolate in turnover (15). However, since the stoichiometry of the modification (i.e., whether full inactivation requires modification of one or both Cys43/dimer) was not determined, these results could not provide additional insight into the apparent asymmetric behavior.

In addition, active-site analyses of the two CoADR structures gave clear evidence for intersubunit cooperation, if not cooperativity, in catalysis. In the 1.5 Å structure of oxidized (FAD, Cys43-SSCoA) *SaCoADR*, a well-ordered chloride ion 3.8 Å from the CoAS-sulfur (chain A) receives hydrogen bonds from several donors including Tyr361'-OH (chain B, 3.1 Å). The position of this chloride ion was taken as the anchor position for the sulfur of the modeled CoAS-II that represents the CoASH product formed on attack of (CoAS)₂ by Cys43-S⁻. A second conserved Tyr (Tyr419', chain B) is 4.2 Å from Cys43-S_γ (chain A), but the Tyr361'-OH—Cl⁻ interaction, in particular, suggested that the latter served the primary role in protonation of the departing CoAS-II thiolate. This working conclusion came into question with the structural analysis of the 2.3 Å *BaCoADR* EH₂·CoASH-NAD(P)H complex, which provides evidence for a reduced enzyme form in which Cys42 adopts an alternate, external conformation. Though not supportive of either Cys42-S⁻ → FAD charge-transfer or in-line nucleophilic attack on the CoAS-I sulfur of (CoAS)₂, this Cys42-S⁻

¹Abbreviations: CoADR, coenzyme A-disulfide reductase; GR, glutathione reductase; *SaCoADR*, *Staphylococcus aureus* coenzyme A-disulfide reductase; *BaCoADR*, *Bacillus anthracis* coenzyme A-disulfide reductase; (CoAS)₂, coenzyme A-disulfide; EH₂, two-electron reduced enzyme; CoAS-I and GS-I, assigned halves of coenzyme A-disulfide and GSSG corresponding to the second CoASH and GSH products, respectively, during catalytic reduction; MMTS, methyl methanethiolosulfonate; EtVC-CoA, α,β-unsaturated ethyl ester-containing CoAS-mimetic inhibitor; MeVS-CoA, methyl vinyl sulfone-containing CoAS-mimetic inhibitor; PhVS-CoA, phenyl vinyl sulfone-containing CoAS-mimetic inhibitor; VSI, phenyl vinyl sulfone-containing inhibitor of cruzain.

interacts strongly with Tyr367'-OH (3.0 Å) and, in particular, Tyr425'-OH (2.9 Å) (equivalent to *SaCoADR* Tyr361' and Tyr419' respectively), suggesting that the latter in fact serves as the primary proton donor.

Given the structural equivalence of Tyr425 and human GR His467, the essential acid-base catalyst in GS-I protonation (16), kinetic analyses were performed on *BaCoADR* and the corresponding Tyr→Phe mutants to further elucidate the catalytic importance of Tyr367 and Tyr425 (2). Compared to a wild-type activity of $k_{\text{cat}} = 27 \text{ s}^{-1}$, the Y367F and Y425F mutants exhibited k_{cat} values of 7 s⁻¹ (26%) and 0.9 s⁻¹ (3%) with NADH and (CoAS)₂ respectively, with no activity reported for the Y367,425F double mutant. These data suggest that while Tyr367 (*SaCoADR* Tyr361) does play a cryptic role as alternate proton donor, Tyr425 is the primary acid-base catalyst (Scheme 2).

Kinetic parameters determined by stopped-flow initial velocity are very similar for *Sa-* and *BaCoADR*, with $k_{\text{cat}} = 27\text{--}29 \text{ s}^{-1}$, $K_m(\text{NADPH})$ ca. 1 μM, and $K_m[(\text{CoAS})_2] = 2\text{--}6 \mu\text{M}$; *BaCoADR* differs primarily in that it exhibits dual NAD(P)H specificity. However, in stopped-flow studies in which an alternate disulfide substrate, MMTS ($K_m^{\text{app}} = 78 \mu\text{M}$ and $k_{\text{cat}} = 6.4 \text{ s}^{-1}$, with wild-type *SaCoADR*), was used (9), the Y361F mutant was actually found to be more efficient ($k_{\text{cat}}/K_m = 2.2 \times 10^5 \text{ M}^{-1}\text{s}^{-1}$) than wild-type enzyme ($k_{\text{cat}}/K_m = 8.2 \times 10^4 \text{ M}^{-1}\text{s}^{-1}$); Y419F and Y361,419F mutants were only 3–5% as efficient ($k_{\text{cat}}/K_m = 2.1\text{--}4.0 \times 10^3 \text{ M}^{-1}\text{s}^{-1}$) as wild-type enzyme. It is important to note that only the internal redox step, i.e., the reduction of Cys43-SSCH₃ by E(FADH₂) that results in CH₃SH formation, requires a proton donor in MMTS turnover (Ref. 9, Scheme 4); with (CoAS)₂ both internal and external (attack of Cys43 on CoAS-I) steps require proton donors.

While the case for intersubunit cooperation in CoADR is therefore supported by both structural and kinetic studies, the question remains as to whether the redox asymmetry seen with *SaCoADR* in particular is translated to the catalytic mechanism. If it is, are Tyr361 and/or Tyr419 important in intersubunit communication? Early studies on mercuric ion reductase (17) strongly supported active-site communication in the dimeric enzyme and led to an alternating sites hypothesis for catalysis. Although the catalytic core has spectroscopic and NADP(H) binding properties identical to those of the full-length protein, the high-resolution crystal structure was not informative (18) on the mechanism of functional asymmetry. *Plasmodium falciparum* thioredoxin reductase is another Disulfide Reductase subgroup enzyme for which intersubunit cooperativity was considered in early work (19). While heterodimers of wild-type enzyme and either C88A or C535A mutants are ca. 50% active with thioredoxin, the wild-type/C88, 535A heterodimer is inactive. Recent studies with the flavin oxidoreductase LuxG (20) and with three bacterial biotin carboxylases (21) provide detailed kinetic and structural evidence for half-sites-reactivity.

In the interest of evaluating the roles of the *SaCoADR* Tyr residues, the role of intersubunit cooperativity in catalysis, and the possible link between Tyr361 and/or Tyr419 and this functional asymmetry, we have taken several approaches. First, we determined the catalytic properties of the *SaCoADR* wild-type/C43S heterodimer and the high-resolution structure of the C43S mutant. Second, we performed reductive titrations on each of the Tyr→Phe mutants and determined their crystal structures. Finally, we also determined the crystal structures for the *SaCoADR* enzymes as inhibited by each of the three different Michael acceptor-containing CoAS-mimetics used in the recent CoADR inhibition study (15). Taken together, the results provide a perspective on intersubunit cooperation in CoADR and on inhibition of this as yet unexploited drug target that establishes a platform for probing the thiol-based redox networks in *S. aureus*, *B. anthracis*, and other pathogens (6).

EXPERIMENTAL PROCEDURES

Materials

NADPH and NADP⁺ were purchased from Boehringer Mannheim or Sigma-Aldrich. Adenosine 2',5'-diphosphate agarose was purchased from Sigma. (CoAS)₂ was either purchased from Fluka or prepared as described previously (15). All other chemicals, as purchased from sources described previously (9), were of the best grades available.

Expression and Purification of Wild-Type and Mutant SaCoADRs

Full-length wild-type and mutant (Y361F, Y419F, Y361,419F, and C43S) *SaCoADR* proteins were expressed and purified as previously described (9, 13). Standard spectrophotometric *SaCoADR* activity assays and anaerobic titrations were performed as previously described for *BaCoADR* (2). The following extinction coefficients were used (in M⁻¹cm⁻¹): NADPH, 6200 at 340 nm; NADP⁺, 18,000 at 260 nm; (CoAS)₂, 33,600 at 260 nm; and wild-type *SaCoADR*, 12,800 at 452 nm (13).

Co-Expression and Purification of Wild-Type/C43S *SaCoADR* Heterodimers in *Escherichia coli* C41(DE3)

The procedure for co-expression and purification of *SaCoADR* homo- and heterodimers followed the general protocol described by Krnajski et al. (19). *E. coli* C41(DE3) cells were transformed with an Amp^r plasmid containing the wild-type *cdr* with an N-terminal *Strep*-tag and a Cm^r plasmid encoding the C43S mutant (N-terminal His-tag). The protocol for large-scale growth and expression was essentially as described by Wallen et al. (9), but with both Amp and Cm supplementation of the growth media. Cell-free extracts were processed as in Luba et al. (13), including both ammonium sulfate fractionation and affinity chromatography with adenosine 2',5'-diphosphate agarose. The enriched total *SaCoADR* pool (ca. 125 mg of *SaCoADR*, based on *A*₄₅₀), in 20 mM Tris-HCl, 50 mM sodium phosphate, pH 8.0, containing 4 M NaCl, was applied to a Ni-NTA Superflow (Qiagen) column equilibrated in the sodium phosphate buffer containing 0.5 M NaCl. Some *SaCoADR* was collected in the flow-through, presumably the *Strep*-tagged wild-type homodimer, and the bound enzyme was eluted with a gradient from 0→250 mM imidazole in the phosphate/NaCl buffer. Approximately 90 mg of *SaCoADR*, presumably heterodimer plus C43S homodimer, resulted at this stage. When this pool was applied directly to a *StrepTactin* column, a large volume containing presumed C43S homodimer flowed through the column. Elution, with the desthiobiotin-containing buffer provided by the vendor, gave a small amount of presumed wild-type/C43S heterodimer. A yield of ca. 3.6 mg of purified *SaCoADR* *Strep*/His-tagged wild-type/C43S heterodimer was estimated by *A*₄₅₂.

Crystallizations

Crystals of C43S, Y361F, Y419F, and Y361,419F *SaCoADR* were obtained, largely following the protocol for wild-type enzyme (14). For the C43S mutant, the optimal condition was 31% PEG 600, 0.4 M MgCl₂, and 0.1 M HEPES, pH 7.2, containing 1.3 mM NADP⁺ and 0.4 mM (CoAS)₂. The Tyr361 and Tyr419 mutants behaved similarly, in the absence of (CoAS)₂. Optimal conditions were 35–37% PEG 600, 0.3–0.4 M MgCl₂, and 0.1 M HEPES, pH 7.5, plus 1.3 mM NADP⁺. The best Y361,419F mutant crystals were obtained in a nearly identical protocol, but with 27% PEG 600 and 0.4 M MgCl₂ at pH 7.2. Growth and handling of crystals for data collection followed the procedures published for wild-type *SaCoADR* (14). For preparation of co-crystals of wild-type *SaCoADR* with the three Michael acceptor-containing CoAS-mimetics [prepared as described previously (15)], the enzyme was first reduced using a 10-fold molar excess of NADPH:enzyme to ensure proper inhibitor binding, followed immediately by the addition of a 20:1 molar ratio of each

of the respective inhibitors. After a 1-h incubation on ice, the reduced enzyme-inhibitor complex was buffer exchanged into 10 mM HEPES, pH 7.2, using a 30 kDa MWCO Amicon concentrator, and subsequently concentrated to >10 mg/mL. Sitting drop, vapor diffusion crystallization experiments were performed as previously detailed (14). Crystal nucleation formed within 3 days, growing into large crystals after 5 days. Crystals were looped and flash frozen in liquid nitrogen in preparation for X-ray data collection.

Data Collection, Structure Solution, and Refinements

X-ray diffraction data for all *SaCoADR* mutants were collected either in-house (C43S, Y361F) on a Rigaku Saturn-92 CCD detector as described for native *BaCoADR* (2) or at beamlines X25 (Y419F) and X26C (Y361,419F) of the National Synchrotron Light Source, using ADSC Quantum-315 and Quantum-4 CCD detectors, respectively. Data sets were indexed, integrated, and scaled in d*TREK (22), with model building and refinements being carried out using CNS (23) and the 1.5 Å wild-type *SaCoADR* structure (PDB entry 1YQZ) as the starting model. Final refinements were performed using TLS (24) plus restrained refinement in REFMAC5 (25), with COOT (26) being applied for manual rebuilding and addition of waters. X-ray diffraction data for the inhibitor complexes were collected at the Advanced Photon Source at Argonne National Labs using the SER-CAT ID-23 beamline. Crystals were indexed in the space group P2₁, with unit cells of $a = 76.5 \text{ \AA}$, $b = 64.8 \text{ \AA}$, $c = 94.6 \text{ \AA}$, and $\beta = 105^\circ$, $\alpha, \gamma = 90.0^\circ$. The asymmetric unit was composed of two 51 kDa monomers. Diffraction data were indexed, integrated and scaled using HKL2000 (27). Table 1 summarizes the data collection statistics for all structures. The inhibitor complex structures were phased by molecular replacement using Phaser (28) and the wild-type *SaCoADR* structure. Positive density was found in the $F_o - F_c$ SA-omit maps for the inhibitors which were covalently bound to Cys43 in the active site. Ligand models and parameter files were generated using the ProDRG server and JLigand (29). Structures were refined using simulated annealing, torsion angle, and *B*-factor refinement using the Phenix software suite (30). Manual refinement of protein residues and inhibitor models was completed using COOT. Refinement statistics for all models are summarized in Table 2.

RESULTS

Spectral and Redox Properties of *SaCoADR* Tyr Mutants

Luba et al. (13) reported the results for dithionite and NADPH titrations of wild-type and C43S *SaCoADR*. With dithionite, the first equiv/FAD clearly reduces each Cys43-SSCoA in each subunit of the wild-type dimer as evidenced by a stoichiometric decrease in flavin fluorescence, with only a minor change in the absorbance spectrum. With the second equiv of dithionite/FAD, the flavin is stoichiometrically reduced. Importantly, it should be noted that no EH₂-like charge-transfer intermediate is observed at 1 equiv of dithionite/FAD. Moreover, the same titration with wild-type *BaCoADR* (2) also fails to reveal any EH₂-like charge-transfer intermediate at 1 equiv/FAD, giving instead an asymmetric redox intermediate, E(FAD, Cys42-SH)_A/E(FADH₂, Cys42-SSCoA)_B.

The dithionite titration with wild-type *SaCoADR* also demonstrates that the Cys43-SSCoA redox center is effectively fully reduced before flavin reduction is observed, at equilibrium. The difference in redox potentials, $E_2 - E_1$, where E_2 represents reduction of oxidized wild-type *SaCoADR* to the EH₂ (FAD, Cys43-SH) form and E_1 is the redox potential for EH₂ (FAD) → EH₄ (FADH₂) (31), is ca. 90 mV. In this respect *SaCoADR* is similar to NADH peroxidase, a Peroxidase-Oxidase-Reductase subgroup enzyme with a Cys42-sulfenic acid (Cys42-SOH) redox center (32, 33). But, while both nonflavin redox centers (Cys43-SSCoA and Cys42-SOH) are reduced preferentially with dithionite, and with no evidence of

intersubunit redox asymmetry, only NADH peroxidase reveals the characteristic EH₂ charge-transfer interaction.

With this in mind, dithionite titrations were performed with *SaCoADR* Y361F, Y419F, and Y361,419F mutants. Detailed results are presented for the Y419F mutant (Figure 1) and are very similar to those obtained with the double mutant. Both mutants behave quite differently compared to the wild-type enzyme, in that flavin reduction is observed in even early stages of the titration; however, full flavin reduction is only seen at 2 equiv of dithionite/FAD.

Flavin reduction is linear with equiv dithionite added through ca. 1.1 equiv/FAD, and 56% of the total ΔA_{454} is seen at 1 equiv/FAD. In contrast with wild-type enzyme, the extents of reduction (at equilibrium) for the flavin and non-flavin centers in Y419F *SaCoADR* are comparable, demonstrating that Tyr419 plays a major role in contributing to the difference in redox potentials, E₂ – E₁. One explanation, in the absence of a more quantitative analysis, is that Tyr419-OH has a key stabilizing effect on (Cys43-SH + CoASH) in the [Cys43-SSCoA/(Cys43-SH + CoASH)] redox couple, and this is consistent with the structure of the *BaCoADR* EH₂-CoASH-NAD(P)H complex. In this context, the structure of the reduced *BaCoADR* Y425F mutant would be quite relevant.

With NADPH, the earlier work of Luba et al. (13) showed that titration of wild-type *SaCoADR* was also biphasic, but in a manner strongly supportive of intersubunit redox asymmetry. In contrast to reduction with dithionite, the first equiv of NADPH/FAD clearly gives significant flavin reduction; however, only one flavin/dimer is reduced. The second flavin/dimer is not reduced (at equilibrium) on addition of 2.4 equiv NADPH/FAD. The redox scheme (Scheme 1) proposed to account for these observations is provided above (see the Introduction). NADPH titration of Y419F *SaCoADR* (Figure 1) also shows flavin reduction in early stages of the experiment. However, in contrast to wild-type *SaCoADR*, full (100%) formation of the E(FADH₂-NADP⁺, Cys43-SSCoA) intermediate is observed at 1 equiv of NADPH/FAD. The strong FADH₂-NADP⁺ charge-transfer band centered at 750 nm is very similar to that observed with C43S *SaCoADR* on NADPH titration (13) and is, at the same time, qualitatively different from that seen in the wild-type *SaCoADR* experiment. As the second equiv of NADPH/FAD is added, there are saturable, stoichiometric changes in absorbance at 454 and 750 nm, and the presence of excess (beyond 1 equiv/FAD) NADPH is clearly indicated at 340 nm. As NADP⁺ binding to the wild-type *SaCoADR* EH₂ form is associated with stoichiometric changes in A₄₅₂ (13), we interpret this phase as representing partial displacement of bound NADP⁺ in the presence of excess NADPH. A similar observation was made in NADPH titrations of C43S *SaCoADR*. However, it appears as if only a small fraction of enzyme molecules reflect this NADPH effect, as addition of NADPH to 7.6 equiv/FAD gives little if any further change in A₄₅₂. Two additional observations can be made: 1) there is no spectral evidence for any intersubunit redox asymmetry on NADPH titration of the Y419F mutant, in dramatic contrast to the behavior of wild-type *SaCoADR*, and 2) while the absorbance changes brought on in the presence of excess NADPH could reflect intramolecular conversion of some E(FADH₂-NADP⁺, Cys43-SSCoA) (EH₂') to E(FAD-NADPH, Cys43-SH): a) this would clearly be substoichiometric, and b) we have no direct evidence for Cys43-SSCoA reduction in the Y419F titration with NADPH; the spectral course is very similar to that for C43S *SaCoADR*. The crystal structure clearly shows 2 CoAS-/dimer, present as the respective Cys43-SSCoA disulfides, in the Y419F mutant. The NADPH titration behavior of Y361F *SaCoADR* is quite similar to that of wild-type enzyme, and that of the Y361,419F double mutant is very similar to that described for the Y419F mutant.² Given that Tyr419 is structurally equivalent with His439,

²The crystal structure of the Y361,419F double mutant indicates that both Cys43-SSCoA per asymmetric unit are partially reduced (ca. 50%). As with the *BaCoADR* and *BaCoADR-RHD* structures, however, this is attributed to synchrotron reduction. The Y361,419F enzyme as purified contains two Cys43-SSCoA disulfides per dimer.

the very important acid-base catalyst required for GS-I protonation in *E. coli* GR (34), the kinetic analysis of the GR H439A mutant also demonstrated an altered, rate-limiting intramolecular electron transfer from that E(FADH₂-NADP⁺) intermediate to the redox-active Cys42-Cys47 disulfide.

Specific Activities of Recombinant SaCoADR Homo- and Heterodimers

Recombinant wild-type *SaCoADR* gives specific activities of 29–34 units/mg ($k_{cat} = 25\text{--}29 \text{ s}^{-1}$) in the standard spectrophotometric assay (13). The C43S enzyme has only ca. 0.03% activity relative to wild-type *SaCoADR*. If the intersubunit redox asymmetry observed on NADPH titration is translated to half-the-sites reactivity in the catalytic cycle, the wild-type/C43S heterodimer would be expected to have the same specific activity as wild-type homodimer. Co-expression of wild-type and C43S constructs in *E. coli* C41(DE3) cells resulted in *Strep*-tagged wild-type homodimers, His-tagged C43S homodimers, and *Strep*/His-tagged wild-type/C43S heterodimers. Affinity purification over 2',5'-ADP agarose, Ni-NTA, and *StrepTactin* resins gave ca. 3.6 mg of wild-type/C43S heterodimer. Specific activities in the standard assay were found to be: 1) wild-type homodimer, 25 units/mg; 2) C43S homodimer, 0.3 units/mg; and 3) wild-type/C43S heterodimer, 11 units/mg. The heterodimer is ca. 44% as active as wild-type homodimer; this result is consistent with full-site reactivity in wild-type *SaCoADR*. On this basis we conclude that the intersubunit redox asymmetry is not reflected in any half-the-sites catalytic activity.

Crystal Structures of SaCoADR C43S and Tyr Mutants

The absence of covalently-bound CoAS- in C43S CoADR was originally demonstrated by mass spectrometry (13). As expected, both dithionite and NADPH titrations led directly to stoichiometric flavin reduction, yielding the E(FADH₂-NADP⁺) complex in the latter case. The structure of C43S *SaCoADR* has now been determined to 1.7 Å resolution and refined to an R_{free} value of 19.2%. The overall tertiary structures of wild-type and C43S enzyme are very similar, with an all-atom rmsd of 0.12 Å. The prime interest is residue 43 and its environment, including the residues of the CoAS-binding cleft. No density corresponding to CoAS- is observed in the mutant. Figure 2 gives $F_o\text{-}F_c$ SA-omit electron density for the C43S *SaCoADR* active site, including Ser43, Tyr361', Tyr419', and portions of the FAD, together with the refined model. The Ser43 side chain adopts two conformations, and the superposition with the active site of the reduced *BaCoADR*-CoASH-NADH complex reveals that the primary β (“external”) conformation corresponds to that for Cys42-S_γ in the reduced *BaCoADR* structure (2), with optimal Ser43-O_γ—Tyr-OH distances of 2.52 and 2.72 Å, respectively, for Tyr361' and Tyr419'. The secondary α (“internal”) conformation gives a proximal Ser43-O_γ to FAD-C4a distance of 2.9 Å but is unfavorable for interactions with either Tyr. In our analysis of the *BaCoADR* structure, we concluded that the external (now β) conformation resulted from the presence of tightly-bound, reduced CoASH (CoAS-I). The present observation with C43S *SaCoADR*, demonstrating that an external conformation for the isosteric Ser side chain is well populated, indicates that the equivalent Cys43-S_γ conformer may also be populated to a significant extent during catalysis — and in the absence of bound CoASH product. A similar external conformation for Cys44-S_γ in the *E. coli* lipoamide dehydrogenase EH₂ form could correspond to the fluorescent species I identified in dithionite titrations (35). As discussed previously, an α-like conformation for *BaCoADR* Cys42-S[−] is required for both the charge-transfer interaction with the flavin and nucleophilic attack on (CoAS)₂.

In the 1.5 Å resolution wild-type *SaCoADR* structure (14), a chloride ion was identified in the active site, as confirmed by anomalous dispersion data. A strong interaction with Tyr361'-OH (3.1 Å) was described, and this chloride was taken to represent the position of the modeled CoAS-II binding mode. In addition, the external conformation of the Cys42

side chain in the reduced *BaCoADR* complex places Cys42-S γ in contact violation (2.2 Å) with the *SaCoADR* chloride, as determined from a superposition. Though not confirmed by anomalous dispersion, a chloride ion is also found in the same position in each of the mutant structures. While we anticipated that the external β conformer of C43S *SaCoADR* would position Ser43-O γ in contact violation with the chloride, this is not the case. Ser43-O γ in this conformer is shifted relative to Cys42-S γ of the reduced *BaCoADR* complex and is 2.8 Å from the chloride. The observation of this chloride in all mutant structures is generally consistent with the absence of synchrotron reduction — excepting the Y361, 419F double mutant — observed with *SaCoADR* versus *BaCoADR* (2) and *BaCoADR-RHD* (9) crystals.

The CoAS-binding cleft in wild-type *SaCoADR* (14) consists of residues from both segments of the FAD-binding domain (chain A) as well as from the Interface domain (chain B). In particular, the pantetheine-4'-pyrophosphate component is very important to the CoAS-:protein interaction in oxidized wild-type enzyme, with a combination of salt bridges, hydrogen-bonding interactions, and hydrophobic contacts involving the pantothenic acid moiety. Even the bound CoASH of the reduced *BaCoADR* complex remains well ordered (2), with the analogous protein contacts preserved. We expected that the absence of the large, extended CoAS- in C43S *SaCoADR* could also lead to rearrangements within the cleft, proximal to the FAD in the active site. Figure 3 gives an overlay for wild-type and C43S *SaCoADR*, focusing on several residues known to interact with bound CoAS- in the cleft. There are two significant differences noted within the cleft. The Lys427' side chain normally interacts through a salt bridge with the 4'-phosphopantetheine moiety of bound CoAS-; in the C43S mutant, two conformations are observed for Lys427'. One superimposes very well with the same residue in the wild-type structure, even though CoAS- is absent in the mutant. The second conformer is stabilized by a new hydrogen-bonding interaction with Gln19-O $\epsilon 1$. Second, with similar resolutions of 1.7 and 1.5 Å, there are 11 additional waters in the CoAS-binding cleft of the C43S CoADR structure, relative to wild-type. These waters take the place of the bound CoAS-, either replacing the adenosine moiety (two waters) or other CoAS- components (nine waters) more proximal to Ser43. In human erythrocyte GR, a structural analysis showed that NADPH binding physically displaced 14 waters (16); in both GR and CoADR, bound water molecules mimic the polar groups of the respective adenine nucleotide and may contribute to the favorable entropic component for ligand binding.

The structures of Y361F and Y419F *SaCoADR* mutants have been determined to resolutions of 1.8 and 1.5 Å, respectively ($R_{\text{free}} = 21.0$ and 19.7%). All-atom rmsd values are 0.08–0.1 Å from comparisons with wild-type enzyme, confirming the absence of major structural differences. Both active sites of both asymmetric units contain oxidized Cys43-SSCoA redox centers, even after exposure to synchrotron radiation during data collection. There is no specific perturbation in the juxtaposition of Cys43-SSCoA and FAD that would indicate unfavorable $\text{FADH}_2 \rightarrow \text{Cys43-SSCoA}$ electron transfer. Considering the 40-fold reduction in $k_{\text{cat}}/K_m(\text{MMTS})$ (9) and the altered redox properties observed in titrations with the NADPH substrate, both with Y419F *SaCoADR*, and the dramatically reduced activity observed with (CoAS)₂ for the equivalent Y425F mutant of *BaCoADR* (2), the Y419F *SaCoADR* structure confirms that these are not due to global structural changes in the oxidized enzyme.

The structure of the Y361,419F double mutant, determined to 1.5 Å resolution ($R_{\text{free}} = 20\%$), reveals partial reduction (ca. 50%) of both Cys43-SSCoA per asymmetric unit.² As the behavior of the double mutant in both MMTS reduction kinetics and NADPH titrations is very similar to that of the Y419F mutant, we interpret these catalytic and redox properties as a primary consequence of the Tyr419 replacement. The absence of activity in the (CoAS)₂ reduction assay with the equivalent *BaCoADR* double mutant, compared with the

residual activity observed with the Y425F mutant, reflects the role of *BaCoADR* Tyr367' as a cryptic proton donor.

Crystal Structures of *SaCoADR*-Inhibitor Complexes

Following on the successful development of irreversible inhibitors of cysteine proteases such as cathepsin K (36) and cruzain (37) — targeting the respective active-site cysteine residues with electrophilic Michael acceptor-containing substrate analogs — the Strauss laboratory recently demonstrated that a similar strategy can be used for the irreversible inhibition of *SaCoADR* (15). In their study, Michael acceptor-containing CoAS-mimetics were prepared as electrophilic traps for the active-site Cys43 residue; this was accomplished by replacing the thiol of CoASH with one of three different electron-withdrawing groups, resulting in CoAS- analogs that contained either an α,β-unsaturated ethyl ester (EtVC-CoA), a methyl vinyl sulfone (MeVS-CoA), or a phenyl vinyl sulfone (PhVS-CoA) moiety, respectively (Scheme 3). These mechanism-based inhibitors operate in a two-step process that involves reversible binding (K_i ca. 40 nM for PhVS-CoA) followed by slow (k_{inact} ca. 0.02 s⁻¹) conjugate addition of the *SaCoADR* Cys43-S⁻ to the inhibitor. As the crystal structures of cathepsin K and cruzain complexed with the respective inhibitors accelerated structure-based drug design programs in both cases (36, 37), we undertook structural analyses of *SaCoADR* complexed with each of three CoAS-mimetics. Moreover, we hoped that such complex structures would provide further insight into the roles of Tyr361' and Tyr419' as proton donors in the *SaCoADR*-catalyzed reaction, considering that protonation of the intermediate that forms on conjugate addition of Cys43-S⁻ to the inhibitor is essential to ensure irreversible, covalent attachment to the enzyme (Scheme 3).

The inhibited enzyme complexes were prepared by incubating *SaCoADR* with NADPH (10 equiv/FAD) and inhibitor (20 equiv/FAD) on ice for one hour. Following buffer exchange and crystallization, synchrotron data sets were collected for complexes with PhVS-CoA, MeVS-CoA, and EtVC-CoA. The structures were determined to resolutions of 1.8 Å ($R_{free} = 20.2\%$), 2.0 Å ($R_{free} = 22.6\%$), and 2.4 Å ($R_{free} = 21.8\%$) (Table 2). Again, the overall tertiary structures are very comparable to that of oxidized (Cys43-SSCoA) *SaCoADR*, with all-atom rmsd values for the respective dimers of 0.11–0.16 Å.

Figure 4 gives the $F_o - F_c$ SA-omit map contoured at 1.2s, for the active-site region of the *SaCoADR*—MeVS-CoA complex; this map illustrates the accuracy of the final refined model and is representative of those calculated for each complex. Each of the final refined models includes one FAD and one inhibitor molecule per active site (Figure 5). As the asymmetric unit corresponds to the biological dimer, it is clear that inhibitor is bound in both active sites per enzyme molecule, with full occupancy. In combination with the activity data for the wild-type/C43S *SaCoADR* heterodimer presented above, this observation of full inhibitor occupancy in each subunit supports the conclusion that *SaCoADR* does not operate *via* half-the-sites reactivity. Each inhibitor has formed a covalent attachment between its β-carbon (relative to the electron-withdrawing group) and the enzyme Cys43-S_γ — as expected for a Michael addition of the Cys residue to the inhibitor. Moreover, in all three inhibitor complexes the -dethia-CoA moiety is clearly present in the CoAS-I site — the same site occupied by the Cys43-SSCoA redox center in oxidized *SaCoADR*. We earlier identified an unoccupied cleft adjacent to bound CoAS- (14); in the inhibitor complexes this cleft is also unoccupied and provides ample opportunity for the elaboration of inhibitor structures.

One consideration for the exclusive association with the CoAS-I site is whether the polar sulfone or carboxyl moieties of the inhibitors contribute strongly to productive binding and inactivation. In each of the four cruzain-inhibitor complexes (37), including that with a phenyl vinyl sulfone inhibitor (VSI) structurally equivalent to PhVS-CoA, there are four

hydrogen bonds between one sulfone oxygen (O35) and the protein. These were noted to outweigh other potential interactions and to lock the inhibitor into the observed orientation. Although unproven, it is likely that these same electrostatic interactions contribute to inhibitor binding to cruzain.³ In all three *SaCoADR*-inhibitor complexes, the respective sulfone and carboxyl moieties occupy the chloride binding site described for oxidized *SaCoADR*, which provides hydrogen-bonding interactions with Cys43-N, Tyr361'-OH, and an active-site water molecule. The 1.5 Å resolution structure of oxidized *SaCoADR* identified 12 polar interactions between CoAS- and protein residues; four additional residues provide hydrophobic contacts (14). There are also 13 solvent waters identified as ligands to CoAS-. As indicated in Figure 6 and in Table 3, these protein interactions are conserved — with two exceptions — in the 1.8 Å resolution *SaCoADR*—PhVS-CoA structure. There is no hydrogen bond between Thr15-OH and the pantothenic acid 2'-OH, and Arg22-N_{η2} does not appear to interact directly with the ribose 2'-OH. However, much more significant is the presence of new electrostatic interactions between one of the sulfone oxygen atoms and both Tyr361'-OH (2.5 Å) and Tyr419'-OH (3.2 Å). This environment for the PhVS- moiety resembles that observed in the analogous cruzain-VSI complex. Additionally, there is a hydrophobic interaction between the phenyl ring of the inhibitor and Pro426, which hovers above it. The conformation of the -dethia-CoA moiety of the bound PhVS-CoA inhibitor is essentially identical to that seen for CoAS- in oxidized *SaCoADR*. For example, the adenine base is partially solvent-exposed and interacts *via* a cation-π stacking mode with the Arg22 guanidinium moiety, and the 3'-phosphate and ribose are entirely solvent exposed.

For the cruzain-VSI complex the position of the phenyl ring was determined solely *via* the electrostatic lock on oxygen O35 of the sulfone group (37). There is an end-on interaction with the indole ring of Trp177, but there are no p-stacking interactions. In comparison with the *SaCoADR*—PhVS-CoA complex, the MeVS-CoA inhibitor conserves all 12 polar interactions found with CoAS- in the oxidized enzyme but lacks the Tyr419'-OH interaction with the sulfone oxygen. There are eight solvent waters identified in this LIGPLOT analysis. The EtVC-CoA inhibitor lacks both Ser39 and Asn42 interactions, the carboxyl oxygen has no contact with either Tyr, and only one solvent water (at the resolution of 2.4 Å) is identified. The decrease in the number of interactions moving from PhVS-CoA to MeVS-CoA to EtVC-CoA seems to be borne out by competitive inhibition K_i values determined for these three inhibitors (Table 4) — 0.04 μM, 0.3 μM, and 0.66 μM, respectively (15). The calculated ΔG_i values therefore increase (are less favorable) by 1.7 kcal/mol through the series.

DISCUSSION

CoASH-Based Thiolomes as Targets

The success of *S. aureus* and *B. anthracis* as bacterial pathogens is dependent on the ability of each to circumvent the innate immune system of the human host (38, 39). Low-molecular-weight thiols such as GSH serve as important intracellular redox buffers in bacteria to counter this challenge (40, 41). *S. aureus* and *B. anthracis*, however, are known to lack GSH (12, 42); CoASH and the recently identified bacillithiol (Cys-GlcN-malate) replace it (6, 7). In *E. coli*, the reduced form of GSH is required for all of its known functions, and the Disulfide Reductase subgroup enzyme GR is responsible for NADPH-dependent GSSG reduction (43). Similarly, the Peroxidase-Oxidase-Reductase subgroup enzyme CoADR has been characterized in detail in both *S. aureus* (14) and *B. anthracis* (2) — in our selection of nine NIAID bacterial pathogens, seven have one or more of the

³W.R. Roush, personal communication.

CoADR isoforms. Recently, CoADR has also been shown to be essential for infection of the mammalian host by the “newly-recognized” NIAID pathogen, *Borrelia burgdorferi* (44).

Synchrotron Reduction of Cys-SSCoA Redox Centers, Cys-SH Conformations, and Reaction Coordinates

The stability of the *Sa*CoADR Cys43-SSCoA center to potential synchrotron reduction may be due to the presence of the well-ordered chloride ion 3.8 Å from the CoAS- sulfur (14). Although the chain B CoAS- moiety is less well ordered, electron density for the disulfide remains well defined. In contrast, both *Ba*CoADR Cys42-SSCoA and *Ba*CoADR-RHD Cys44-SSCoA centers are subject to synchrotron reduction, the latter to an extent of ca. 50% (2, 9). As described earlier, the naturally-reduced Cys42-SH side chain of the *Ba*CoADR EH₂-CoASH-NAD(P)H complex adopts a new external conformation in which Cys42-S_γ interacts with both Tyr367'-OH and Tyr425'-OH. While this conformation has been attributed to the tightly bound CoASH product, it may be populated to some extent during catalysis.

In the inactivated structures of *Sa*CoADR presented in this work, Cys43-S_γ adopts the internal conformation seen in the oxidized Cys43-SSCoA enzyme. While this favorable comparison for Cys43-SSCoA and Cys43-SCHR'CH₂SO₂Ph (R' = -dethia-CoA) conformations is anticipated, the nucleophilic attack of Cys43-S⁻ in the catalytic cycle, comparing the natural (CoAS)₂ substrate disulfide with the Michael acceptor-containing CoAS-mimetic, reveals insights into the respective transition states. In the former case, both Cys43-S_γ and the CoAS-I sulfur [of (CoAS)₂] represent divalent sulfur; both atoms exhibit *sp*³ hybridization. In earlier work Rosenfield et al. (45) analyzed crystal structures of small molecules containing divalent sulfur in order to establish preferred directions of nucleophilic attack (e.g., by Cys43-S⁻ on CoAS-I sulfur). For nonbonded S···S intermolecular contacts, the nucleophilic center tends to approach the complementary sulfur ca. along the extension of one of the covalent bonds to that electrophilic center, i.e., in plane. This S_N2-like displacement involves no change in bond order about CoAS-I sulfur (Scheme 2). The same applies as Cys43-S⁻ attacks the divalent sulfur center of MMTS.

However, the electrophilic carbon center of the Michael acceptor-containing CoAS-mimetics is *sp*² hybridized with trigonal planar geometry relative to its -dethia-CoA, -H, and =C_α neighbors. This raises several stereochemical and conformational questions for the reaction coordinate. First, does the proton addition to C_α follow a *syn* or *anti* stereochemical course? Second, presuming the -dethia-CoA moiety serves as a conformational anchor in the addition reaction, the =C_α-SO₂Ph moiety will change position in the reaction coordinate, as the C_β electrophilic center assumes tetrahedral, *sp*³ character. This may contribute additional transition-state stabilization in the conjugate addition reaction, which is 80-fold faster (*k*_{ass}) for R = -SO₂Ph than for -SO₂Me (15). The inactivation kinetics with R = -CO₂Et, -SO₂Me, and -SO₂Ph can be compared with the reaction kinetics for *Sa*CoADR with both (CoAS)₂ (13) and with MMTS (Table 3) (9). From the individual kinetic parameters and specificity constants (inhibitor potencies), values for the binding energies and free energies of activation have been calculated for these reactions.

Nucleophilic Additions of Thiols to Disulfides versus Michael Acceptors

For the inactivation of cruzain with one series of phenyl-containing vinyl sulfone inhibitors, Brinen et al. (37) reported values for *k*_{ass} (see Table 4) ranging from 10⁵–10⁷ M⁻¹s⁻¹ at room temperature. In complexes with each of four inhibitors, the electrostatic contributions of hydrogen bond interactions with at least one sulfone oxygen lock each inhibitor in the observed orientation. For the VSI inhibitor, *k*_{ass} = 3.2 × 10⁵ M⁻¹s⁻¹ corresponds to ΔG[‡]_T = 9.9 kcal/mol; increasing length for the spacer connecting the sulfone component with the

P1' phenyl appears to have a favorable effect on k_{ass} . To the extent that reported IC₅₀ values represent competitive K_i parameters, this also reflects a favorable effect on ΔG_i for increased inhibitor length. The reaction between cruzain Cys25 and VSI in fact mimics that for the formation of the “tetrahedral intermediate” in protease catalysis (46). While the VSI phenyl group is proximal to the P1' binding site, with the addition of atoms between the phenyl ring and the sulfone moiety contributing favorably to k_{ass} (and thus, to ΔG^{\ddagger}_T), these observations suggest that the peptidyl component must move in the transition state. Although direct evidence that the sulfone group is locked in place on VSI binding is lacking, this remains the working conclusion.³

The k_{ass} values determined for cruzain (Cys25) (37) and *SaCoADR* (Cys43) (15) to similar phenyl vinyl sulfone-based Michael acceptor-containing mimetics (VSI and PhVS-CoA, respectively, as corrected for different reaction temperatures) differ by ca. 16-fold in favor of the cruzain reaction. This corresponds to a $\Delta\Delta G^{\ddagger}_T$ of ca. 2 kcal/mol, in part reflecting the non-natural conformational change about C_B of the PhVS-CoA electrophilic center in the reaction coordinate for *SaCoADR* Cys43 reaction. The k_{ass} value of $4 \times 10^4 \text{ M}^{-1}\text{s}^{-1}$ determined for *SaCoADR* and PhVS-CoA at 37°C is ca. two orders of magnitude lower than $k_{cat}/K_m[(\text{CoAS})_2]$ ($9.0 \times 10^6 \text{ M}^{-1}\text{s}^{-1}$) measured at 25°C. While this corresponds to a $\Delta\Delta G^{\ddagger}_T$ of ca. 3.6 kcal/mol (not correcting for different reaction temperatures) favoring reduction of (CoAS)₂ over reaction with the CoAS-mimetic, the calculated ΔG_i for PhVS-CoA is 3 kcal/mol more favorable than ΔG_s calculated for (CoAS)₂.

The rates of reaction for an organic thiol with compounds similar to those in the cruzain series have been reported, but only as relative rates (47). Szajewski and Whitesides (48) have analyzed the reactions of organic thiols, both with free GSSG and with protein-SSCH₃ (and other) disulfides. The observed correlation between thiol p*K*_a and rate of nucleophilic attack on GSSG was interpreted in support of a simple S_N2 transition state, as suggested by crystallographic analyses cited previously (45), yielding a preferred direction of approach for a sulfur nucleophile to a disulfide along that S-S axis. There is significant negative charge on all three S atoms in this transition state (S_{nuc}···S_c···S_{lg}), but it is concentrated on S_{nuc} and S_{lg}. While rates of GSSG reduction in these model studies are generally slow, the reaction rates of thiols with papain Cys25-SSCH₃, for example, approach 8300 M⁻¹s⁻¹ (= k_1) for 2-mercaptoethanol (49). There is no evidence from this work to suggest deviation from the S_N2 displacement reaction previously described for thiol-disulfide interchange; local factors contributing to Cys-S⁻ leaving group acidity, rather than steric effects of protein structure, dominate the reactivity as observed.

Inhibitor Design Potential

The observation that the covalent inhibitors — detailed in the co-crystal structures reported here with *S. aureus* CoADR — leave unoccupied space in the CoAS-II binding cleft has been noted. Additionally, it is clear that Tyr361' and Tyr419' assist in locking down the inhibitors, as outlined in Figures 5B and 6B. Thus, there is good evidence that the existing compounds provide a strong starting point for novel inhibitor design. Indeed, next generation inhibitors could be designed to exploit the open space in the CoAS-II binding cleft, and in so doing provide increased binding affinity and selectivity for the target enzymes in a range of host organisms. If such compounds could be developed and validated, they could contribute both basic and translational leads in the search for new clinical approaches to several NIAID priority pathogens, such as *S. aureus*, *B. anthracis*, and *B. burgdorferi*.

Acknowledgments

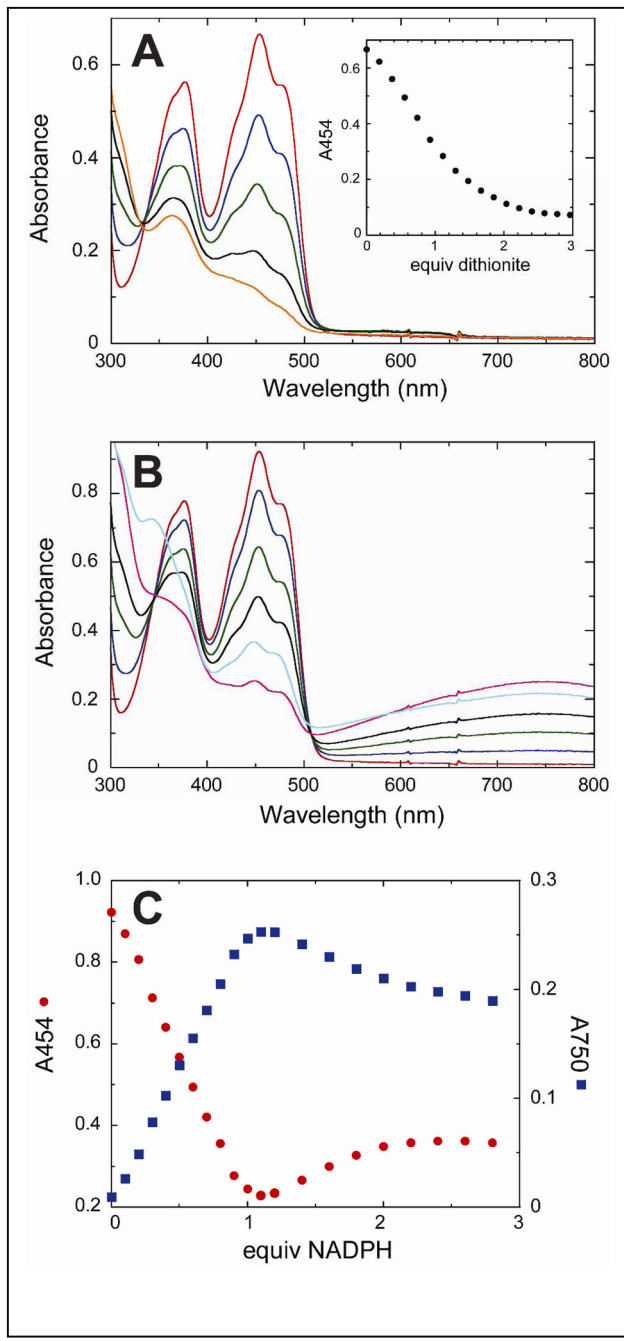
We especially thank Dr. Conn Mallett and Dr. Derek Parsonage for their leading roles in protein expression and crystallography with the *SaCoADR* mutants.

References

1. www.narcis.nl/research/RecordID/OND1345442/Language/en.
2. Wallen JR, Paige C, Mallett TC, Karplus PA, Claiborne A. Pyridine nucleotide complexes with *Bacillus anthracis* coenzyme A-disulfide reductase: a structural analysis of dual NAD(P)H specificity. *Biochemistry*. 2008; 47:5182–5193. [PubMed: 18399646]
3. Argyrou A, Blanchard JS. Flavoprotein disulfide reductases: advances in chemistry and function. *Prog Nucleic Acid Res Mol Biol*. 2004; 78:89–142. [PubMed: 15210329]
4. Atkinson HJ, Babbitt PC. An atlas of the thioredoxin fold class reveals the complexity of function-enabling adaptations. *PLoS Comput Biol*. 2009; 5:e1000541. [PubMed: 19851441]
5. Chi BK, Gronau K, Maeder U, Hessling B, Becher D, Antelmann H. *S*-bacillithiolation protects against hypochlorite stress in *Bacillus subtilis* as revealed by transcriptomics and redox proteomics. *Mol Cell Proteomics*. 2011; 10:M111.009506. [PubMed: 21749987]
6. Parsonage D, Newton GL, Holder RC, Wallace BD, Paige C, Hamilton CJ, Dos Santos PC, Redinbo MR, Reid SD, Claiborne A. Characterization of the *N*-acetyl- α -D-glucosaminyl L-malate synthase and deacetylase functions for bacillithiol biosynthesis in *Bacillus anthracis*. *Biochemistry*. 2010; 49:8398–8414. [PubMed: 20799687]
7. Newton GL, Rawat M, La Clair JJ, Jothivasan VK, Budiarto T, Hamilton CJ, Claiborne A, Helmann JD, Fahey RC. Bacillithiol is an antioxidant thiol produced in Bacilli. *Nat Chem Biol*. 2009; 5:625–627. [PubMed: 19578333]
8. Ojha S, Meng EC, Babbitt PC. Evolution of function in the “two dinucleotide binding domains” flavoproteins. *PLoS Comput Biol*. 2007; 3:e121. [PubMed: 17658942]
9. Wallen JR, Mallett TC, Boles W, Parsonage D, Furdui CM, Karplus PA, Claiborne A. Crystal structure and catalytic properties of *Bacillus anthracis* CoADR-RHD: implications for flavin-linked sulfur trafficking. *Biochemistry*. 2009; 48:9650–9667. [PubMed: 19725515]
10. Warner MD, Lukose V, Lee KH, Lopez K, Sazinsky MH, Crane EJ III. Characterization of an NADH-dependent persulfide reductase from *Shewanella loihica* PV-4: implications for the mechanism of sulfur respiration via FAD-dependent enzymes. *Biochemistry*. 2011; 50:194–206. [PubMed: 21090815]
11. Haveman SA, DiDonato RJ Jr, Villanueva L, Shelobolina ES, Postier BL, Xu B, Liu A, Lovley DR. Genome-wide gene expression patterns and growth requirements suggest that *Pelobacter carbinolicus* reduces Fe(III) indirectly via sulfide production. *Appl Environ Microbiol*. 2008; 74:4277–4284. [PubMed: 18515480]
12. delCardayre SB, Stock KP, Newton GL, Fahey RC, Davies JE. Coenzyme A disulfide reductase, the primary low molecular weight disulfide reductase from *Staphylococcus aureus*: Purification and characterization of the native enzyme. *J Biol Chem*. 1998; 273:5744–5751. [PubMed: 9488707]
13. Luba J, Charrier V, Claiborne A. Coenzyme A-disulfide reductase from *Staphylococcus aureus*: evidence for asymmetric behavior on interaction with pyridine nucleotides. *Biochemistry*. 1999; 38:2725–2737. [PubMed: 10052943]
14. Mallett TC, Wallen JR, Karplus PA, Sakai H, Tsukihara T, Claiborne A. Structure of coenzyme A-disulfide reductase from *Staphylococcus aureus* at 1.54 Å resolution. *Biochemistry*. 2006; 45:11278–11289. [PubMed: 16981688]
15. van der Westhuyzen R, Strauss E. Michael acceptor-containing coenzyme A analogues as inhibitors of the atypical coenzyme A disulfide reductase from *Staphylococcus aureus*. *J Am Chem Soc*. 2010; 132:12853–12855. [PubMed: 20738089]
16. Karplus PA, Schulz GE. Substrate binding and catalysis by glutathione reductase as derived from refined enzyme - substrate crystal structures at 2 Å resolution. *J Mol Biol*. 1989; 210:163–180. [PubMed: 2585516]

17. Miller SM, Massey V, Williams CH Jr, Ballou DP, Walsh CT. Communication between the active sites in dimeric mercuric ion reductase: an alternating sites hypothesis for catalysis. *Biochemistry*. 1991; 30:2600–2612. [PubMed: 2001350]
18. Ledwidge R, Patel B, Dong A, Fiedler D, Falkowski M, Zelikova J, Summers AO, Pai EF, Miller SM. NmerA, the metal binding domain of mercuric ion reductase, removes Hg²⁺ from proteins, delivers it to the catalytic core, and protects cells under glutathione-depleted conditions. *Biochemistry*. 2005; 44:11402–11416. [PubMed: 16114877]
19. Krnajski Z, Gilberger TW, Walter RD, Müller S. Intersubunit interactions in *Plasmodium falciparum* thioredoxin reductase. *J Biol Chem*. 2000; 275:40874–40878. [PubMed: 11022050]
20. Nijvipakul S, Ballou DP, Chaiyen P. Reduction kinetics of a flavin oxidoreductase LuxG from *Photobacterium leiognathi* (TH1): half-sites reactivity. *Biochemistry*. 2010; 49:9241–9248. [PubMed: 20836540]
21. Mochalkin I, Miller JR, Evdokimov A, Lightle S, Yan C, Stover CK, Waldrop GL. Structural evidence for substrate-induced synergism and half-sites reactivity in biotin carboxylase. *Protein Sci*. 2008; 17:1706–1718. [PubMed: 18725455]
22. Pflugrath JW. The finer things in X-ray diffraction data collection. *Acta Cryst*. 1999; D55:1718–1725.
23. Brunger AT, Adams PD, Clore GM, DeLano WL, Gros P, Grosse-Kunstleve RW, Jiang JS, Kuszewski J, Nilges M, Pannu NS, Read RJ, Rice LM, Simonson T, Warren GL. Crystallography & NMR system: a new software suite for macromolecular structure determination. *Acta Cryst*. 1998; D54:905–921.
24. Winn MD, Isupov MN, Murshudov GN. Use of TLS parameters to model anisotropic displacements in macromolecular refinement. *Acta Cryst*. 2001; D57:122–133.
25. Murshudov GN, Vagin AA, Dodson EJ. Refinement of macromolecular structures by the maximum-likelihood method. *Acta Cryst*. 1997; D53:240–255.
26. Emsley P, Cowtan K. Coot: model-building tools for molecular graphics. *Acta Cryst*. 2004; D60:2126–2132.
27. Otwinowski Z, Minor W. Processing of X-ray diffraction data collected in oscillation mode. *Methods Enzymol*. 1997; 276:307–326.
28. McCoy AJ, Grosse-Kunstleve RW, Adams PD, Winn MD, Storoni LC, Read RJ. Phaser crystallographic software. *J Appl Cryst*. 2007; 40:658–674. [PubMed: 19461840]
29. Schuttelkopf AW, van Aalten DM. PRODRG: a tool for high-throughput crystallography of protein-ligand complexes. *Acta Cryst*. 2004; D60:1355–1363.
30. Adams PD, Afonine PV, Bunkoczi G, Chen VB, Davis IW, Echols N, Headd JJ, Hung LW, Kapral GJ, Grosse-Kunstleve RW, McCoy AJ, Moriarty NW, Oeffner R, Read RJ, Richardson DC, Richardson JS, Terwilliger TC, Zwart PH. PHENIX: a comprehensive Python-based system for macromolecular structure solution. *Acta Cryst*. 2010; D66:213–221.
31. Matthews RG, Williams CH Jr. Measurement of the oxidation-reduction potentials for two-electron and four-electron reduction of lipoamide dehydrogenase from pig heart. *J Biol Chem*. 1976; 251:3956–3964. [PubMed: 6467]
32. Poole LB, Claiborne A. Interactions of pyridine nucleotides with redox forms of the flavin-containing NADH peroxidase from *Streptococcus faecalis*. *J Biol Chem*. 1986; 261:14525–14533. [PubMed: 3095321]
33. Poole LB, Claiborne A. The non-flavin redox center of the streptococcal NADH peroxidase. I Thiol reactivity and redox behavior in the presence of urea. *J Biol Chem*. 1989; 264:12322–12329. [PubMed: 2501302]
34. Rietveld P, Arscott LD, Berry A, Scrutton NS, Deonarain MP, Perham RN, Williams CH Jr. Reductive and oxidative half-reactions of glutathione reductase from *Escherichia coli*. *Biochemistry*. 1994; 33:13888–13895. [PubMed: 7947797]
35. Wilkinson KD, Williams CH Jr. Evidence for multiple electronic forms of two-electron-reduced lipoamide dehydrogenase from *Escherichia coli*. *J Biol Chem*. 1979; 254:852–862. [PubMed: 33177]
36. McGrath ME, Klaus JL, Barnes MG, Bromme D. Crystal structure of human cathepsin K complexed with a potent inhibitor. *Nat Struct Biol*. 1997; 4:105–109. [PubMed: 9033587]

37. Brinen LS, Hansell E, Cheng J, Roush WR, McKerrow JH, Fletterick RJ. A target within the target: probing cruzain's P1' site to define structural determinants for the Chagas' disease protease. *Structure*. 2000; 8:831–840. [PubMed: 10997902]
38. Kobayashi SD, DeLeo FR. An update on community-associated MRSA virulence. *Curr Opin Pharmacol*. 2009; 9:545–551. [PubMed: 19726228]
39. Passalacqua KD, Bergman NH. *Bacillus anthracis*: interactions with the host and establishment of inhalational anthrax. *Future Microbiol*. 2006; 1:397–415. [PubMed: 17661631]
40. Fahey RC. Novel thiols of prokaryotes. *Annu Rev Microbiol*. 2001; 55:333–356. [PubMed: 11544359]
41. Zuber P. Management of oxidative stress in *Bacillus*. *Annu Rev Microbiol*. 2009; 63:575–597. [PubMed: 19575568]
42. Nicely NI, Parsonage D, Paige C, Newton GL, Fahey RC, Leonardi R, Jackowski S, Mallett TC, Claiborne A. Structure of the type III pantothenate kinase from *Bacillus anthracis* at 2.0 Å resolution: implications for coenzyme A-dependent redox biology. *Biochemistry*. 2007; 46:3234–3245. [PubMed: 17323930]
43. Toledano MB, Kumar C, Le Moan N, Spector D, Tacnet F. The system biology of thiol redox system in *Escherichia coli* and yeast: differential functions in oxidative stress, iron metabolism and DNA synthesis. *FEBS Lett*. 2007; 581:3598–3607. [PubMed: 17659286]
44. Eggers CH, Caimano MJ, Malizia RA, Kariu T, Cusack B, Desrosiers DC, Hazlett KRO, Claiborne A, Pal U, Radolf JD. The coenzyme A disulphide reductase of *Borrelia burgdorferi* is important for rapid growth throughout the enzootic cycle and essential for infection of the mammalian host. *Mol Microbiol*. 2011; 82:679–697. [PubMed: 21923763]
45. Rosenfield RE, Parthasarathy R, Dunitz JD. Directional preferences of nonbonded atomic contacts with divalent sulfur. 1 Electrophiles and nucleophiles. *J Am Chem Soc*. 1977; 99:4860–4862.
46. Brak K, Kerr ID, Barrett KT, Fuchi N, Debnath M, Ang K, Engel JC, McKerrow JH, Doyle PS, Brinen LS, Ellman JA. Nonpeptidic tetrafluorophenoxyethyl ketone cruzain inhibitors as promising new leads for Chagas disease chemotherapy. *J Med Chem*. 2010; 53:1763–1773. [PubMed: 20088534]
47. Reddick JJ, Cheng J, Roush WR. Relative rates of Michael reactions of 2'-(phenethyl)thiol with vinyl sulfones, vinyl sulfonate esters, and vinyl sulfonamides relevant to vinyl sulfonyl cysteine protease inhibitors. *Org Lett*. 2003; 5:1967–1970. [PubMed: 12762698]
48. Szajewski RP, Whitesides GM. Rate constants and equilibrium constants for thiol-disulfide interchange reactions involving oxidized glutathione. *J Am Chem Soc*. 1980; 102:2011–2026.
49. Shaked Z, Szajewski RP, Whitesides GM. Rates of thiol-disulfide interchange reactions involving proteins and kinetic measurements of thiol pK_a values. *Biochemistry*. 1980; 19:4156–4166. [PubMed: 6251863]
50. www.rcsb.org/pdb/ligand/ligandsummary.do?hetId=COA.
51. www.rcsb.org/pdb/ligand/ligandsummary.do?hetId=VS1&sid=1F29.
52. Bieth JG. Theoretical and practical aspects of proteinase inhibition kinetics. *Methods Enzymol*. 1995; 248:59–84. [PubMed: 7674947]
53. Fersht, A. *Structure and Mechanism in Protein Science*. W.H. Freeman and Company; New York: 1999.

**Figure 1.**

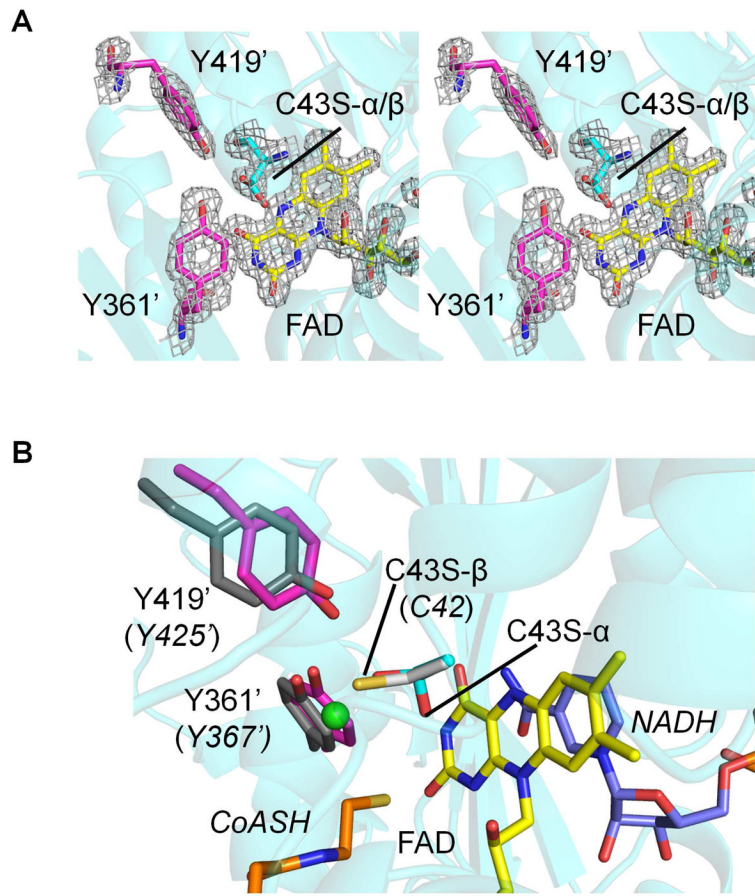
Dithionite and NADPH titrations of Y419F *SaCoADR*. (A) The enzyme (53.6 μ M, in 1.0 mL of 50 mM potassium phosphate, pH 7.0, plus 0.5 mM EDTA) was titrated with a 7.5 mM solution of dithionite. Spectra shown, in order of decreasing absorbance at 454 nm, correspond to the addition of 0 (red), 0.56 (blue), 0.93 (green), 1.48 (black), and 2.04 (orange) equiv of dithionite/FAD. Inset: Absorbance change at 454 nm *versus* added dithionite. The end point corresponds to 1.69 equiv of dithionite/FAD. (B) The enzyme (42.7 μ M, prepared as above) was titrated with a 5.4 mM solution of NADPH. Spectra shown, in order of decreasing absorbance at 454 nm, correspond to the addition of 0 (red), 0.2 (blue), 0.4 (green), 0.6 (black), and 1.0 (magenta) equiv of NADPH/FAD. The increase

in A_{454} on addition of a second equiv (cyan) of NADPH/FAD corresponds to partial formation of the $\text{EH}_2\text{-NADPH}$ species given in Scheme 1. (C) Absorbance changes at 454 (red circles) and 750 nm (blue squares) *versus* added NADPH. The end points (ΔA_{454}) correspond to 1.0 and 2.05 equiv of NADPH/FAD.

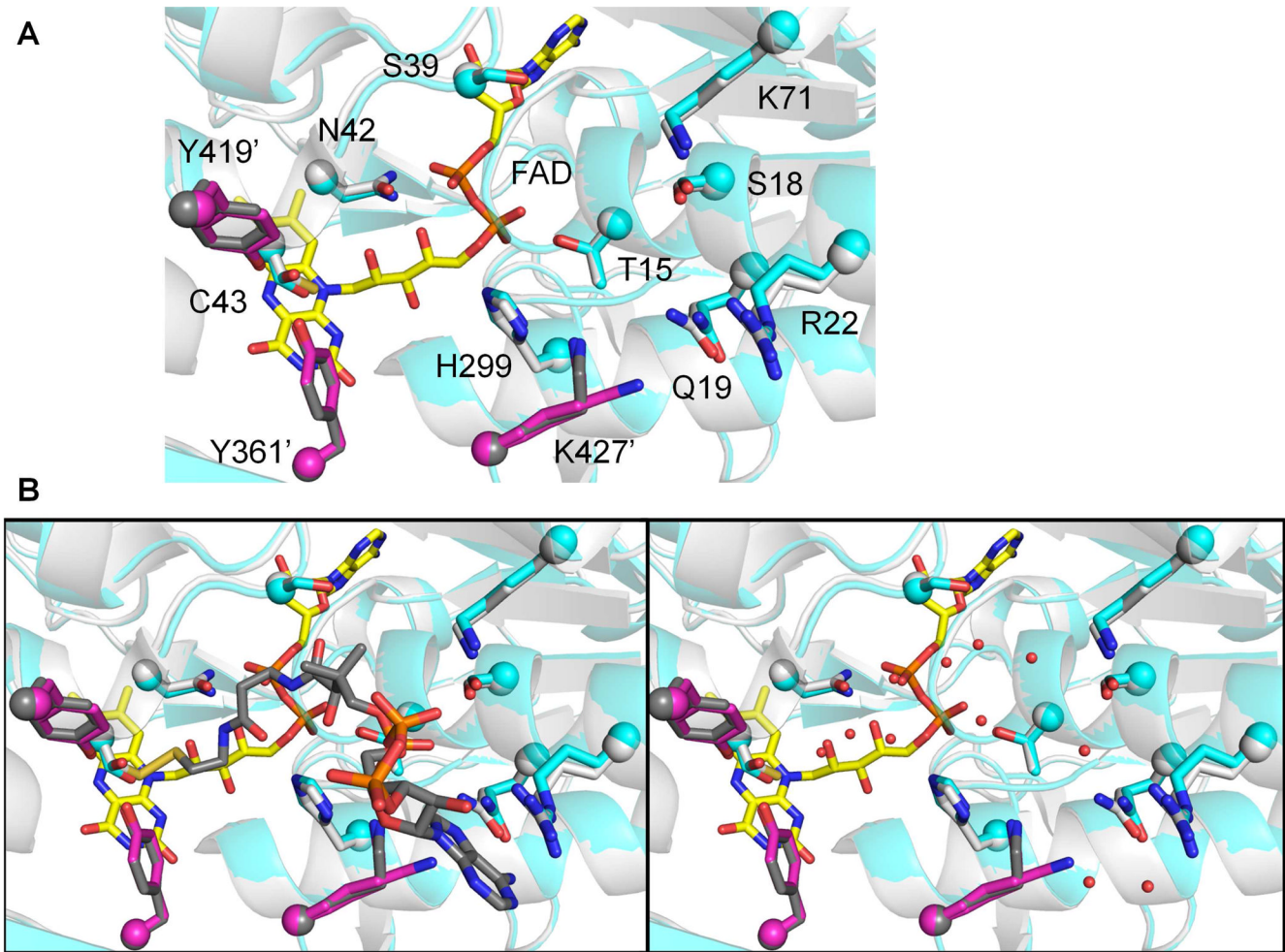
\$watermark-text

\$watermark-text

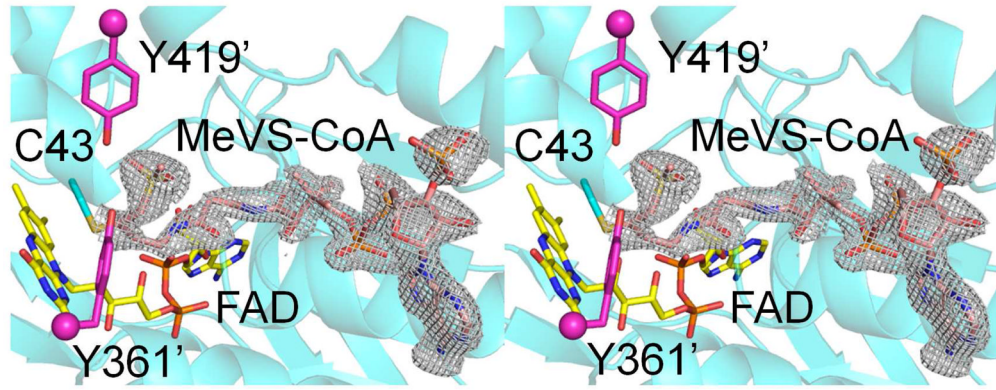
\$watermark-text

**Figure 2.**

(A) Stereoview of the *SaCoADR* C43S mutant, focusing on the active site. The refined model includes FAD (color-coded by atom type, with portions omitted for clarity), both conformations (α and β) of the Ser43 side chain, and Tyr361' and Tyr419'. An $F_o - F_c$ SA omit map is shown contoured at 1.5 σ . All protein residues are color-coded by atom type, with C α and side chain carbon atoms colored cyan and magenta for chain A and chain B of the homodimer, respectively. Chain A secondary structural elements are rendered as 50% transparent. (B) Superposition of the *SaCoADR* C43S mutant and the *BaCoADR* EH₂-CoASH-NADH complex. The refined model for the reduced *BaCoADR* complex includes FAD, CoASH (carbon atoms colored orange), NADH (carbon atoms color-coded slate blue), Cys42-SH, and active-site Tyr residues 367' and 425'. Color-coding for *SaCoADR* is as in (A), above, with the active-site chloride ion represented as a green sphere. Side chain carbon atoms for *BaCoADR* chain A and chain B residues are colored light gray and dark gray, respectively. Most notable is that the external, β -conformation of the Ser43 side chain in the mutant adopts the same conformation as that of Cys42-SH in the reduced *BaCoADR* structure. Secondary structural elements are rendered as 50% transparent.

**Figure 3.**

(A) Overlay of the wild-type and C43S mutant *SaCoADR* crystal structures, focusing on the CoAS-binding cleft. In addition to FAD, Cys43-S-, and Tyr431' and Tyr419', key residues known to interact with the CoAS- moiety within the active-site cleft are indicated for the wild-type structure, with carbon atoms colored light gray and dark gray for chains A and B as before. CoAS- has been omitted from the model for clarity. Chain A and B carbon atoms for the mutant are colored cyan and magenta, as before. Notably, side chains lining the cleft maintain the conformations found in the wild-type structure, even in the absence of bound CoAS-. Lys427', however, adopts two conformations in the C43S mutant structure attributed to this absence. Secondary structural elements are rendered as 50% transparent. (B, left) Overlay from (A), above, but including the full Cys43-SSCoA model (CoAS- carbon atoms now in dark gray). (B, right) Same view as in (B, left), but now including the new bound solvent waters (red spheres) that are recruited into the cleft in the absence of CoAS-. CoAS- has been omitted from the wild-type *SaCoADR* model as in (A), above.

**Figure 4.**

Stereoview of the inhibited *SaCoADR*—MeVS-CoA complex, focusing on the active site. The presentation is similar to that given in Figure 2A for the C43S mutant but includes Cys43 of the wild-type enzyme as modified with MeVS-CoA. Chain A and B protein residues are color-coded, with carbon atoms in cyan and magenta, respectively. FAD and bound MeVS-CoA are color-coded by atom type, with FAD carbon atoms in yellow and MeVS-CoA carbon atoms in orange. An $F_o - F_c$ SA-omit map contoured at 1.2σ is shown for MeVS-CoA. Secondary structural elements are represented as transparent.

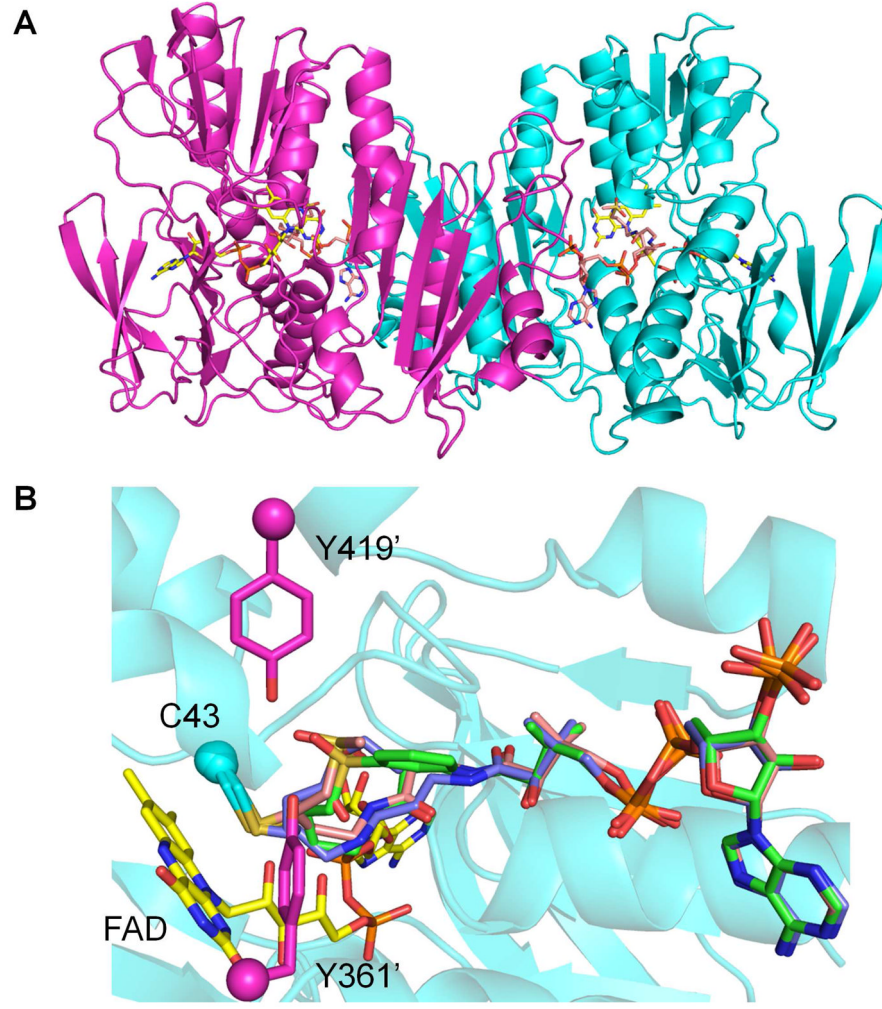
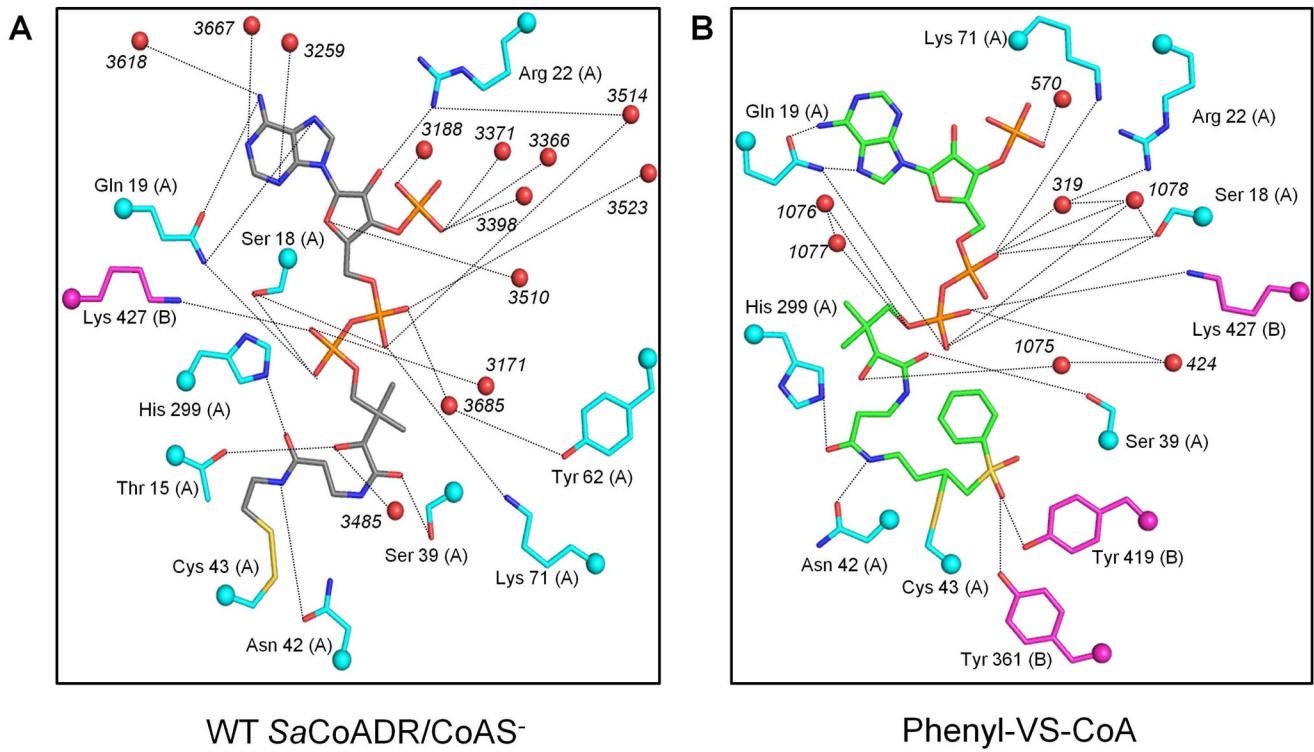
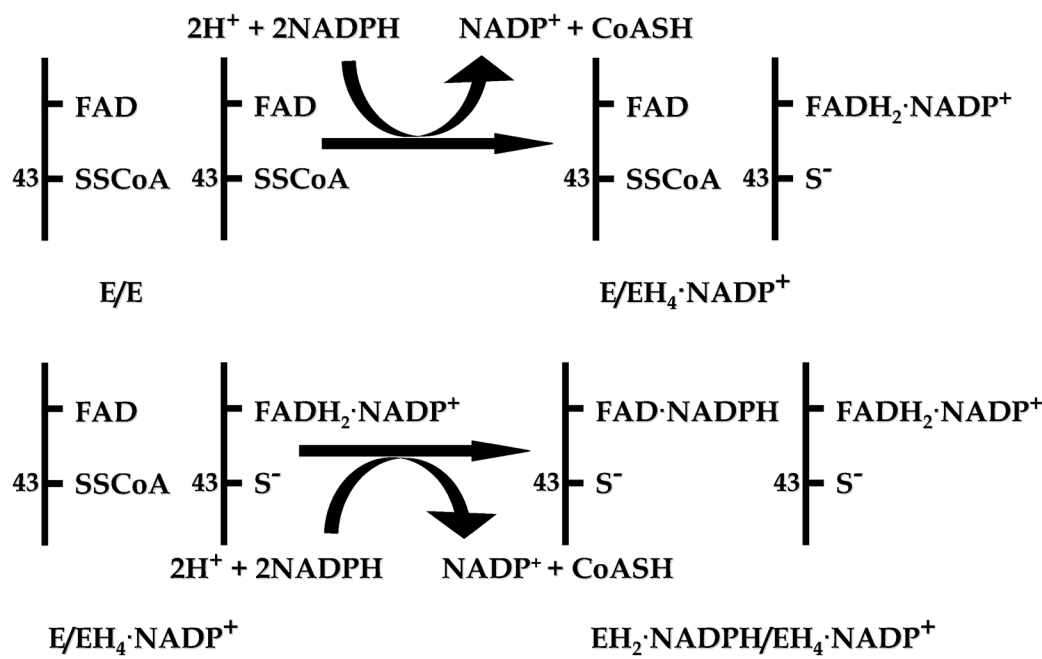


Figure 5.

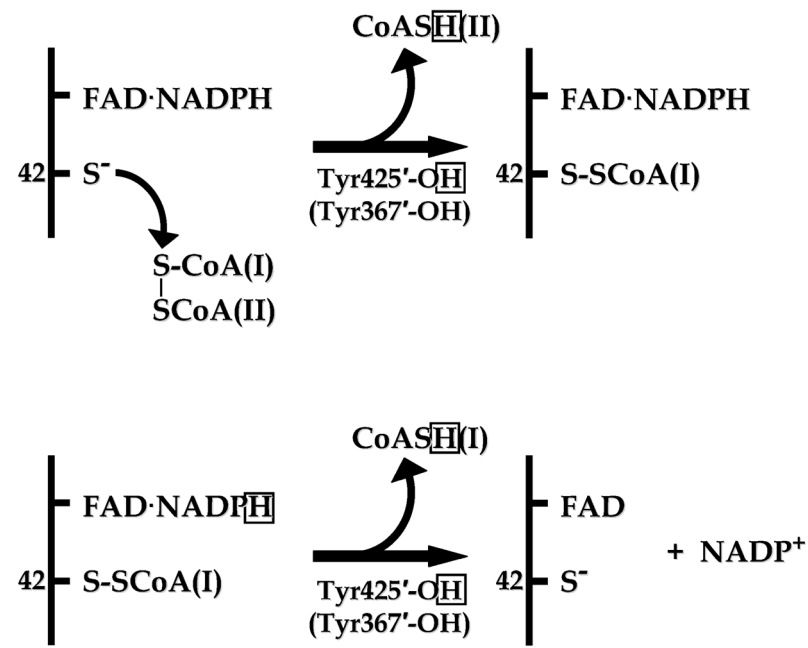
(A) Asymmetric unit for the inhibited *SaCoADR*—MeVS-CoA complex, corresponding to the biological dimer. Each active site includes one Cys43—MeVS-CoA adduct. All elements are color-coded as in Figure 4. (B) Overlay of the three inhibitor-bound *SaCoADR* complexes, showing covalently bound MeVS-CoA (carbon atoms colored pink), PhVS-CoA (carbon atoms colored green), and EtVC-CoA (carbon atoms colored blue) inhibitors. The MeVS-CoA complex conserves all 12 polar interactions seen with bound CoAs- in wild-type *SaCoADR*. Tyr361'-OH interacts with one sulfone oxygen in both MeVS-CoA and PhVS-CoA complexes, and Tyr419'-OH interacts similarly in the PhVS-CoA complex structure.

**Figure 6.**

(A) LIGPLOT representation of polar protein and solvent water interactions with CoAS⁻ in the wild-type *SaCoADR* crystal structure. These interactions are generally conserved in all three (MeVS-CoA, PhVS-CoA, and EtVC-CoA) inhibitor bound crystal structures, as detailed in the text. (B) LIGPLOT representation of polar protein interactions with the PhVS-CoA inhibitor in the structure of that complex. A number of residues lining the active-site cleft provide electrostatic and hydrogen-bonding interactions with the -dethia-CoA moiety and with one sulfone oxygen of the inhibitor. Additional hydrogen-bonding interactions with the -dethia-CoA portion are indicated with ordered water molecules. All color coding is as in Figure 5B.

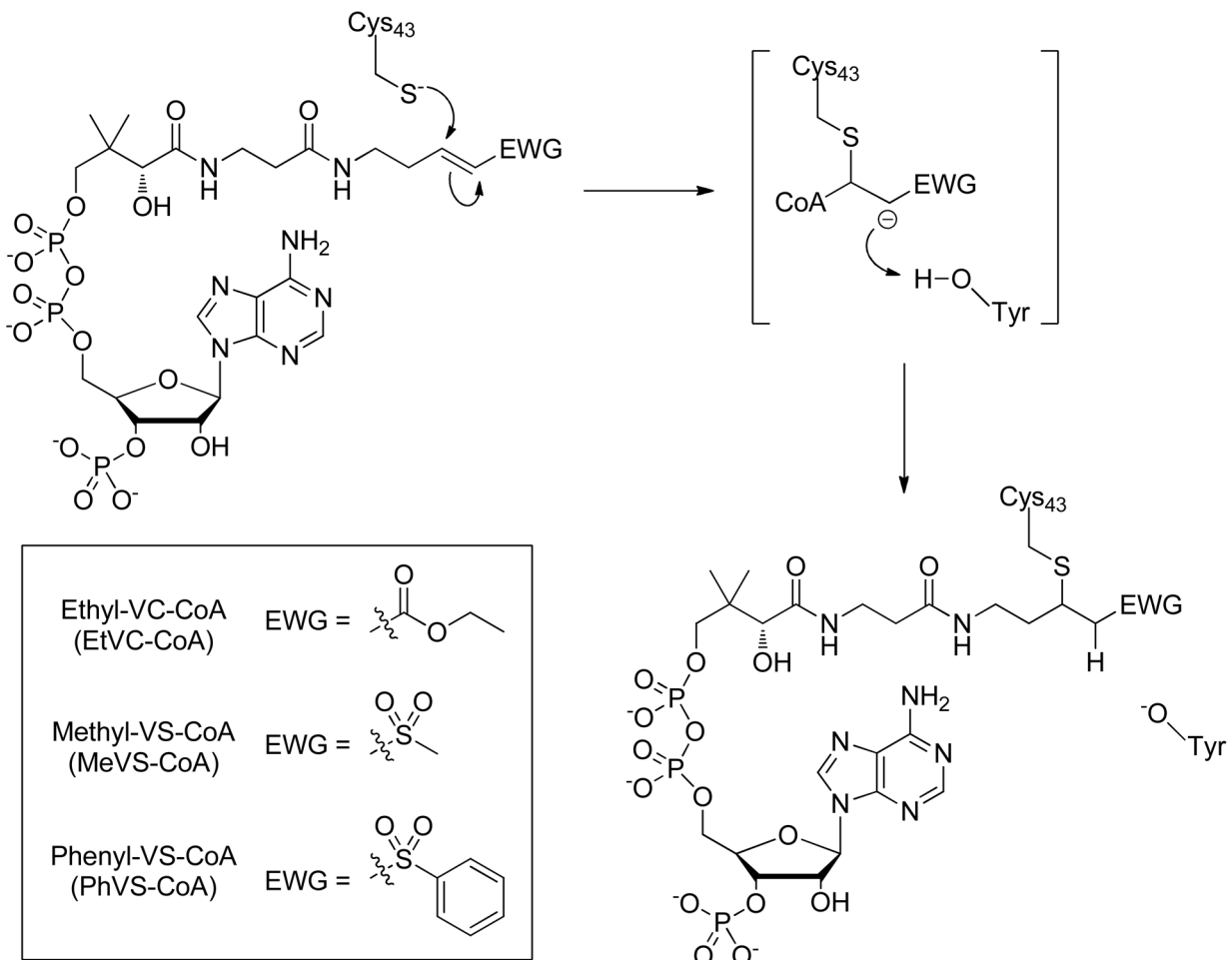


Scheme 1.
Reductive intermediates on NADPH titration of *SaCoADR*.



Scheme 2.

Proton donors and their proposed roles in *BaCoADR*.

**Scheme 3.**

Mechanism-based inhibition of *SaCoADR* by covalent modification of the active site Cys₄₃ through nucleophilic addition to the Michael acceptor-containing CoAS-mimetics.

Table 1

Data Collection Statistics for Wild-type *SaCoADR* Complexes with the Three Michael Acceptor-containing CoAS-Mimetics and for *SaCoADR* C43S and Tyr Mutants

	C43S	Y361F	Y419F	Y361,419F	EIVC-CoA	MeVS-CoA	PhVS-CoA
X-ray source	LAB ^a	LAB	X25 ^b	X26C ^c	APS SER-CAT ID-23 ^d	APS SER-CAT ID-23	APS SER-CAT ID-23
Wavelength (Å)	1.5418	1.5418	1.1000	1.1000	1.0000	1.0000	1.0000
Space group	P21	P21	P21	P21	P21	P21	P21
Cell dimensions							
<i>a, b, c</i> (Å)	76.0, 65.4, 94.5	75.9, 65.1, 94.4	76.2, 65.4, 94.6	76.2, 65.5, 94.7	76.5, 64.8, 94.6	76.5, 64.8, 94.6	76.5, 64.8, 94.6
α, β, γ (°)	90, 105, 90	90, 105, 90	90, 105, 90	90, 105, 90	90, 105, 90	90, 105, 90	90, 105, 90
Resolution (Å)	53.16-1.70 (1.76-1.70) ^e	53.00-1.80 (1.86-1.80)	51.35-1.50 (1.55-1.50)	53.29-1.50 (1.55-1.50)	50.0-2.40 (2.44-2.40)	50.0-2.00 (2.03-2.00)	50.0-1.83 (1.86-1.83)
Unique reflections	98577	82678	137217	140142	33246	62908	79955
Completeness (%)	99.9 (99.9)	99.9 (100)	95.4 (79.8)	97.1 (77.5)	98.1 (97.0)	97.2 (85.2)	97.1 (89.9)
Redundancy	6.3 (4.3)	7.0 (6.8)	7.3 (6.4)	6.9 (5.2)	7.3 (6.4)	4.1 (2.6)	7.3 (5.6)
<i>I</i> / <i>σ</i>	11.0 (3.1)	7.9 (2.7)	17.1 (4.6)	16.0 (4.1)	38.4 (7.6)	24.1 (2.71)	38.1 (3.98)

^aCollected on a Rigaku Saturn-92 CCD detector using Cu Kα radiation from a MicroMax-007 rotating anode X-ray generator.

^bCollected at beamline X25 of the National Synchrotron Light Source using an ADSC Quantum-315 CCD detector.

^cCollected at beamline X26C of the National Synchrotron Light Source using an ADSC Quantum-4 CCD detector.

^dCollected at beamline ID-23 of the Advanced Photon Source using a Marmosaic 300 CCD detector.

^eNumbers in parentheses represent data for the highest-resolution shell.

Table 2

Crystallographic Refinement Statistics for Wild-type *S. australiensis* CoADR Complexes with the Three Michael Acceptor-containing CoAS-Mimetics and for *S. australiensis* C43S and Tyr Mutants

	C43S	Y361F	Y419F	Y361,419F	E1V/C-CoA	MeV/S-CoA	PhV/S-CoA
R-work	0.193 (0.263) ^a	0.185 (0.253)	0.178 (0.272)	0.180 (0.268)	0.164 (0.187)	0.179 (0.262)	0.153 (0.225)
R-free	0.232 (0.318)	0.226 (0.315)	0.201 (0.284)	0.207 (0.275)	0.218 (0.246)	0.226 (0.321)	0.202 (0.362)
Molecules per asymmetric unit (AU)	2	2	2	2	2	2	2
No. of amino acids per AU	874 ^b	874	874	874	874	876 ^c	876
No. of waters per AU	939	1216	1268	1285	226	998	1084
Average <i>B</i> -factors	22.81	22.24	18.18	16.99	33.67	26.69	20.66
Stereoechemical ideality							
Bond length rmsd (Å)	0.030	0.006	0.005	0.005	0.02	0.008	0.01
Bond angle rmsd (°)	2.220	1.047	1.032	1.027	1.816	1.719	1.758
ϕ , ψ preferred (%)	98	97	98	98	94.6	97.5	97
ϕ , ψ allowed (%)	1.7	2.6	1.6	1.6	4.4	2.3	2.6
ϕ , ψ outliers (%)	0.23	0.34	0.34	0.34	1.0	0.20	0.34

^aNumbers in parentheses represent data for the highest-resolution shell.

^b*S. australiensis* CoADR dimer.

^cLys438 included in the final refined model.

Table 3

Polar Interactions with CoAS⁻ and PhVScCoA in Oxidized *SaCoADR* and the *SaCoADR*-inhibitor Complex

Oxidized <i>SaCoADR</i> protein and CoAS ⁻ atoms ^a	D...A (Å)	<i>SaCoADR</i> –PhVScCoA complex protein and PhVScCoA atoms	D...A (Å)
Thr15-O _γ ...CoAS-OAP	2.7	no contact with Thr15	---
Ser18-O _γ ...CoAS-O5A	2.8	Ser18-O _γ ...PhVScCoA-O5A	3.1
Ser18-O _γ ...CoAS-O2A	3.2	Ser18-O _γ ...PhVScCoA-O2A	3.3
Gln19-N _{ε2'} ...CoAS-N7A	2.8	Gln19-N _{ε2'} ...PhVScCoA-N7A	2.8
Gln19-N _{ε2'} ...CoAS-O5A	2.8	Gln19-N _{ε2'} ...PhVScCoA-O5A	3.2
Gln19-O _{ε1'} ...CoAS-N6A	2.9	Gln19-O _{ε1'} ...PhVScCoA-N6A	2.8
Arg22-N _{η2} ...CoAS-O2B	3.1	Arg22-N _{η2} ...WAT319...PhVScCoA-O1A	3.0/2.6
Ser39-O _γ ...CoAS-O9P	2.6	Ser39-O _γ ...PhVScCoA-O9P	3.0
Asn42-O _{δ1} ...CoAS-N4P	3.0	Asn42-O _{δ1} ...PhVScCoA-N4P	2.6
Lys71-N _ε ...CoAS-O2A	2.9	Lys71-N _ε ...PhVScCoA-O1A	3.1
His299-N _{ε2'} ...CoAS-O5P	2.8	His299-N _{ε2'} ...PhVScCoA-O5P	2.7
Lys427'-N _ζ '...CoAS-O4A	2.7	Lys427'-N _ζ '...PhVScCoA-O4A	2.7
Tyr361'-O _η '...PhVScCoA-SO(O35)		Tyr361'-O _η '...PhVScCoA-SO(O35)	2.5
Tyr419'-O _η '...PhVScCoA-SO(O35)		Tyr419'-O _η '...PhVScCoA-SO(O35)	3.2

^a Atom labeling for CoAS⁻ is derived from the Protein Data Bank ligand summary (50). Atom labeling for PhVScCoA is based directly on that for CoAS⁻, with that for O35 of the sulfone group being taken from that for the equivalent sulfone oxygen in the cruzain-VSI complex (37), as described in the text. See also Ref. 51.

Table 4
Kinetic Parameters and Associated Free Energies for *SaCoADR* Catalysis and Inactivation

T = 298 K	K _m	K _{cat}	K _{cat} /K _m	ΔG _s ^a	ΔG _i ^b	ΔG [‡] ^c
(CoAS)₂						
wild-type	3 μM	27 s ⁻¹	9.0 × 10 ⁶ M ⁻¹ s ⁻¹	-7.5 kcal·mol ⁻¹	8.0 kcal·mol ⁻¹	15.5 kcal·mol ⁻¹
MMTS						
wild-type	78 μM	6.4 s ⁻¹	8.2 × 10 ⁴ M ⁻¹ s ⁻¹	-5.6 kcal·mol ⁻¹	10.7 kcal·mol ⁻¹	16.3 kcal·mol ⁻¹
Y361F	47 μM	10.4 s ⁻¹	2.2 × 10 ⁵ M ⁻¹ s ⁻¹	-5.9 kcal·mol ⁻¹	10.2 kcal·mol ⁻¹	16.1 kcal·mol ⁻¹
Y419F	575 μM	1.2 s ⁻¹	2.1 × 10 ³ M ⁻¹ s ⁻¹	-4.4 kcal·mol ⁻¹	12.9 kcal·mol ⁻¹	17.3 kcal·mol ⁻¹
T = 310 K ^d	K _i ^e	K _{inact} (K ₂) ^f	K _{ass} (K ₂ /K _i *) ^g	ΔG _i ^h	ΔG _i ^j	ΔG [‡] ^j
EtVc-CoA	0.66 μM		219 M ⁻¹ s ⁻¹	-8.8 kcal·mol ⁻¹	14.8 kcal·mol ⁻¹	23.6 kcal·mol ⁻¹
MeVc-CoA	0.3 μM		500 M ⁻¹ s ⁻¹	-9.3 kcal·mol ⁻¹	14.3 kcal·mol ⁻¹	23.6 kcal·mol ⁻¹
PhVc-CoA	0.04 μM ^k	(9.4 × 10 ⁻³ s ⁻¹) ^k	4.0 × 10 ⁴ M ⁻¹ s ⁻¹	-10.5 kcal·mol ⁻¹	11.6 kcal·mol ⁻¹	22.1 kcal·mol ⁻¹

^aCalculated assuming K_m = K_d.

^bCalculated directly from k_{cat}/K_m.

^cCalculated from (ΔG[‡]_T-ΔG_S).

^dKinetic parameters taken from Ref. 15.

^eDetermined from competitive inhibition kinetics.

^fThe first-order rate constant, k_{inact} (15) = k₂ (Ref. 52; Scheme X).

^gThe second-order rate constant, k_{ass} (Ref. 52; Scheme IX) can be set = k₂/K_i* in cases where no EI* is observed kinetically. K_i* = K_i.

^hCalculated assuming K_i = K_d.

ⁱCalculated directly from k_{ass}.

^jCalculated from (ΔG[‡]_T-ΔG_i).

^kAs reported by van der Westhuyzen and Strauss (15), the plot of k_{obs} versus [I] is hyperbolic only for the PhVc-CoA inhibitor, allowing determination of k₂ and K_i* only in its case. This value of k₂ is given in parentheses. Free energy parameters are defined as in Ref. 53.